Matter

Article

Surface termination engineering of 2D titanium carbides for light-activated soft robotics applications

Graphical abstract

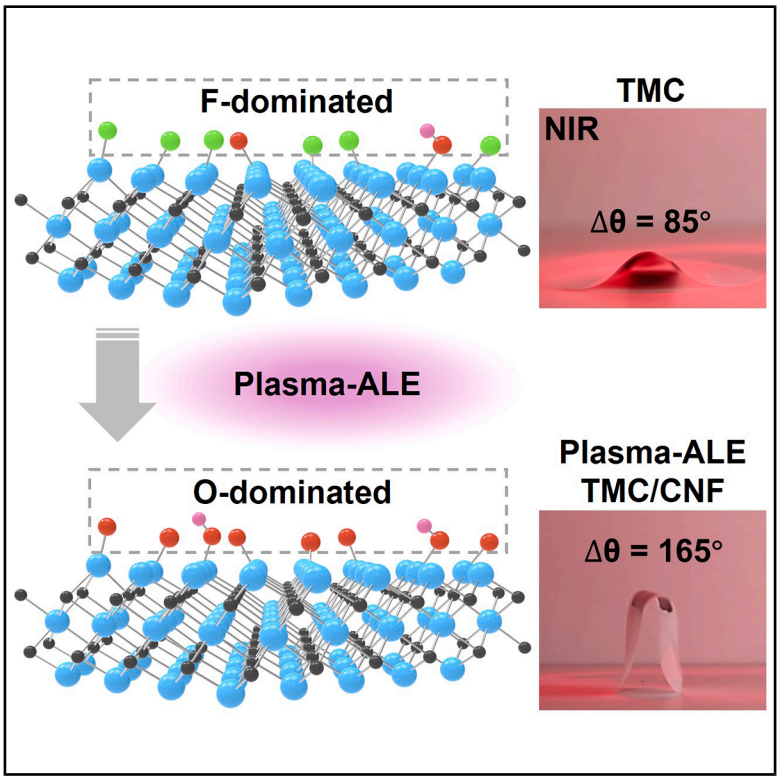

Highlights

- Plasma-ALE converts $Ti_3C_2T_x$ surface from F- to O-dominated terminations
- Plasma-ALE boosts TMC conductivity by 80% and improves photothermal efficiency
- Plasma-ALE-treated TMC/CNF actuators bend 165° and generate 40 mN force under NIR
- Compatible with vacuum filtration and aerosol jet printing for scalable fabrication

Authors

Dhamelyz Silva-Quinones, Xingjian Hu, Brian Cole, ..., Daniel Franke, Aaron D. Franklin, Haozhe Wang

Correspondence

haozhe.wang@duke.edu

In brief

This study introduces plasma-ALE as a precise post-treatment to replace performance-limiting fluorine terminations in $Ti_3C_2T_x$ MXene with oxygen-dominated groups. When combined with cellulose nanofibrils, the engineered material enables light-driven soft actuators with enhanced force and motion. The method supports scalable, programmable robotic structures via both vacuum filtration and aerosol jet printing.

Improvement

Enhanced performance with innovative design or material control

Silva-Quinones et al., 2025, Matter 8, 102264
October 1, 2025
https://doi.org/10.1016/j.matt.2025.102264

CellPress

Please cite this article in press as: Silva-Quinones et al., Surface termination engineering of 2D titanium carbides for light-activated soft robotics applications, Matter (2025), https://doi.org/10.1016/j.matt.2025.102264

Matter

CellPress

Article

Surface termination engineering of 2D titanium carbides for light-activated soft robotics applications

Dhamelyz Silva-Quinones,[1,8] Xingjian Hu,[1,8] Brian Cole,[1] Anna Bethke,[1] Alexander Hool,[1] Yilin Zhao,[1] William Collins,[2] Wubin Bai,[3] Qiangu Yan,[4] Jianjun Wei,[5] Michael D. Dickey,[6] Daniel Franke,[4] Aaron D. Franklin,[1,7] and Haozhe Wang[1,9,*]

[1]Department of Electrical and Computer Engineering, Duke University, Durham, NC 27708, USA
[2]Department of Biology, Duke University, Durham, NC 27708, USA
[3]University of North Carolina at Chapel Hill, Chapel Hill, NC 27514, USA
[4]Forest Products Laboratory, US Department of Agriculture, Madison, WI 53726, USA
[5]Department of Nanoscience, University of North Carolina Greensboro, Greensboro, NC 27401, USA
[6]North Carolina State University, Raleigh, NC 27695, USA
[7]Department of Chemistry, Duke University, Durham, NC 27708, USA
[8]These authors contributed equally
[9]Lead contact
*Correspondence: haozhe.wang@duke.edu
https://doi.org/10.1016/j.matt.2025.102264

PROGRESS AND POTENTIAL Plasma-enabled atomic layer etching (plasma-ALE) is introduced as a precise and scalable method to engineer surface terminations of the transition metal carbide (TMC) $Ti_3C_2T_x$ for high-performance light-driven soft robotics. Traditional synthesis introduces fluorine groups that limit conductivity and photothermal efficiency, impeding actuator performance. The plasma-ALE method replaces these groups with oxygen-containing terminations, boosting conductivity by 80% and significantly enhancing photothermal response. Incorporation of cellulose nanofibrils (CNFs) further improves actuator integrity and water retention. The resulting $Ti_3C_2T_x$/CNF actuators demonstrate exceptional light-driven performance, including 165° bending angle and 40 mN force under near-infrared light. The plasma-ALE technique is compatible with multiple fabrication methods, including vacuum filtration and aerosol jet printing, enabling soft actuators with programmable shapes across length scales. This advancement leads to reconfigurable devices like soft grippers and worm-like robots. The findings demonstrate a pathway toward scalable manufacturing of high-efficiency, multifunctional soft robots, offering promise for next-generation applications in biomedicine, flexible electronics, and environmental sensing.

SUMMARY

The transition metal carbide (TMC) $Ti_3C_2T_x$ features high conductivity, photothermal conversion, and flexibility, making it promising for light-driven soft actuators. However, conventional synthesis often results in fluorine terminations that degrade photothermal efficiency. This study introduces a plasma-enabled atomic layer etching (plasma-ALE) approach to precisely engineer the surface termination of $Ti_3C_2T_x$, transforming the surface chemistry from fluorine-dominated to oxygen-dominated terminations, achieving an 80% conductivity increase and significantly enhanced photothermal efficiency. Incorporating cellulose nanofibrils further improves ALE-treated actuator response under near-infrared light, yielding up to 165° bending and 40 mN force, outperforming other 2D material-based actuators. The plasma-ALE process is compatible with various fabrication methods, including vacuum filtration and aerosol jet printing, enabling scalable designs. Furthermore, plasma-ALE treatment facilitates actuators capable of grasping and locomotion. This work paves the way for advanced surface engineering of TMCs and their integration into multifunctional soft robotic systems.

Please cite this article in press as: Silva-Quinones et al., Surface termination engineering of 2D titanium carbides for light-activated soft robotics applications, Matter (2025), https://doi.org/10.1016/j.matt.2025.102264

INTRODUCTION

Stimuli-responsive actuators have garnered significant attention in diverse fields, including biomimetic robotics, healthcare devices, and human-robot interaction systems, due to their capacity to convert external stimuli (e.g., light, heat, humidity, electricity, magnetism, chemicals) into mechanical energy.[1–5] Within this domain, soft robotics has emerged as an important category, distinguished by its high degree of deformability. The core of soft robotics lies in stimuli-responsive soft materials. Traditionally, these have included dielectric or liquid crystal elastomers, hydrogels, magnetic materials, and shape memory polymers.[6] Recent advancements have brought two-dimensional (2D) materials to the forefront of this field. Starting with graphene, 2D materials have exhibited great potential as stimuli-responsive soft materials due to their large surface-to-volume ratio, mechanical flexibility, and extraordinary electrical and thermal properties, as well as their capacity to transduce diverse external stimuli into functional responses.[7]

Among 2D materials, the transition metal carbide (TMC, also known as MXene), particularly $Ti_3C_2T_x$, has emerged as a promising candidate. $Ti_3C_2T_x$ exhibits high electrical conductivity due to its metallic nature and high density of free electrons, which positively correlates with its photothermal conversion efficiency.[8,9] Proof-of-concept $Ti_3C_2T_x$ actuators have demonstrated rapid light responsiveness, particularly in the near-infrared (NIR) region, and strong force actuation.[3,10–13] The conductivity of $Ti_3C_2T_x$ is significantly influenced by their surface terminations (T_x), which are determined by synthesis and post-processing methods. Recently, minimally intensive layer delamination (MILD) has been the most prevalent and high-output acid etching method for $Ti_3C_2T_x$ synthesis.[14,15] However, $Ti_3C_2T_x$ produced by the MILD method typically contains numerous –F terminations due to the LiF precursor, which is detrimental to electrical conductivity. Therefore, post-treatment following MILD to engineer surface chemistry with desired termination groups is imperative to enhance the performance of light-driven TMC soft robotics.[16–18] Common T_x tailoring methods include heat treatment, solvothermal treatment, and chemical grafting. However, these methods often lack atomic-level processing precision, uniformity, and scalability for prospective industrial workflows, and they are prone to introducing contaminants and defects into the intrinsic Ti_3C_2 structure.[19–21]

Plasma treatment has been demonstrated to effectively alter surface functional groups with high atomic precision. For example, N_2 plasma can increase the photocatalytic activity of TMC by introducing beneficial T_xs.[22] Among T_xs (–F, –OH, =O) of TMC, O-containing terminations have demonstrated higher electrical conductivity.[23,24] Low-power O_2/Ar plasma is ideal for realizing etching and replacement of the T_x functional groups, converting as-fabricated –F into –OH or =O. The mechanisms of O_2 and Ar plasma treatment differ significantly, but there is a synergistic amplification effect when using them as a mixture. O_2 plasma treatment induces chemical modification as O_2 discharges and releases O-containing radicals ($\cdot O_2^-$, $\cdot O_2^{2-}$, $\cdot$OH), replacing original T_x atoms with OH/O^- groups to form an O-dominated surface.[25] Conversely, Ar plasma treatment causes physical etching through strong ion bombardment to remove T_xs.[26] The literature also indicates that adding Ar gas to O_2 plasma increases the density of high-energy electrons and provides more active sites for O-containing functional groups, enhancing the replacing efficiency of O_2 plasma.[27]

Cellulose nanofibrils (CNFs) were added into TMCs to form the TMC/CNF actuation material system. TMC/CNF composites are widely explored due to their synergistic properties. The integration of CNFs into TMC-based materials significantly improves structural integrity, water retention, and thermal management of TMCs, making them ideal for applications in soft robotics, flexible electronics, and adaptive devices. Several studies have demonstrated the effectiveness of TMC/CNF composites in enhancing actuator performance, particularly in response to external stimuli like NIR light.[10,13,28]

In this study, we developed a plasma-enabled atomic layer etching (plasma-ALE) technique to engineer the T_xs of $Ti_3C_2T_x$ (hereafter referred to as TMC). ALE is a top-down method enabling atomic-level modification of TMC surface chemistry. Through O_2/Ar plasma ALE, most of the T_xs of TMC were tailored into –OH and =O, resulting in an 80% increase in electrical conductivity and enhanced photothermal conversion efficiency. Furthermore, we fabricated a bimorph actuator by depositing TMC/cellulose composites onto a polycarbonate (PC) membrane using vacuum filtration. After plasma-ALE treatment, TMC/cellulose soft robotics exhibits a 30% increase in bending angle and a 21% enhancement in bending force under NIR light. This study also validates the compatibility of plasma-ALE treatment with various manufacturing methods and soft robotics systems, with efficacy across multiple scales ranging from millimeters to centimeters.

RESULTS

Surface termination (T_x)engineering by plasma-ALE treatment

To enhance the photothermal performance of TMC, we developed a plasma-assisted ALE process to modify its surface chemistry, converting the T_xs from F-dominated to O-dominated (see Figure 1A). We investigated the optimal O_2:Ar ratio in the plasma-ALE treatment. As shown in Figure 1B, all plasma treatment cases increased the conductivity of TMC films, demonstrating that plasma ALE can effectively remove conductivity-reducing terminations (e.g., –F). Both pure O_2 and pure Ar plasma treatments significantly increased TMC film conductivity, with pure O_2 plasma replacement performing slightly better. It is because pure O_2 plasma replaced –F with =O or –OH, while pure Ar plasma etched most T_xs, converting the material to intrinsic Ti_3C_2. The 80:20 and 20:80 O_2:Ar ratios showed less ideal enhancement compared to pure O_2 or Ar plasma. This demonstrates that insufficient Ar fails to adequately activate high-energy electrons in O_2, while insufficient O_2 leads to low replacement efficiency. These results underscore the importance of balanced gas composition in achieving optimal surface modification. The highest conductivity increase (80% compared to the original TMC film) was achieved by 50:50 Ar:O_2 ratio. This optimal ratio maximized the advantages of both O_2 and Ar plasma etching, with Ar and O_2 plasma synergistic effects, creating an O-dominated surface with improved out-of-plane charge transport by enhancing the density of states and

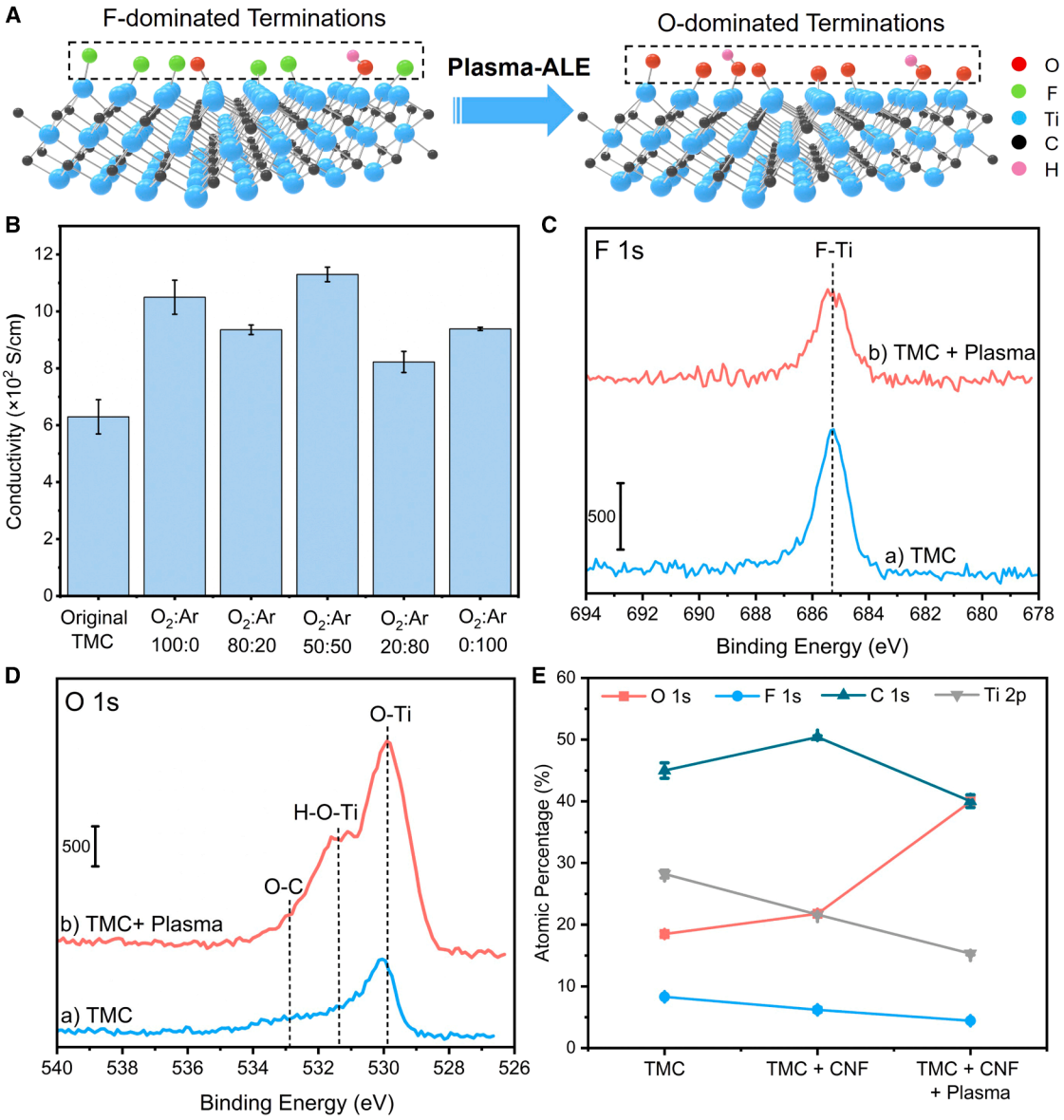

Figure 1. Plasma-ALE surface engineering of TMC

(A) Schematic illustration of the plasma-ALE technique for TMC surface modification.

(B) Electrical conductivity of $Ti_3C_2T_x$ TMC films before and after plasma-ALE treatment with varying Ar:O_2 ratios. Error bars represent standard error of the mean (SEM), n = 3.

(C and D) High-resolution XPS spectra of (C) F 1s and (D) O 1s in TMC and TMC after plasma-ALE treatment.

(E) XPS-derived atomic concentrations in TMC and TMC with cellulose nanofibrils (CNFs) before and after plasma-ALE treatment. Error bars represent standard error of the mean, n = 3.

shifting the Fermi level, resulting in better inter-layer electron mobility and thus overall conductivity in the films of stacked multi-layer MXene.[29] Electrical conductivity is mainly governed by the Ti atoms, which dominate the density of states near the Fermi level.[24] T_xs can alter the electronic structure and thereby influence conductivity. Among them, –F groups exhibit strong electron-withdrawing effects, significantly reducing electron density and conductivity.[23] In contrast, –OH terminations can engage in conjugation resonance, partially increasing the electron density at the metal center.[24] =O terminations also contribute to improved conductivity and notably enhance the Seebeck coefficient and overall thermoelectric performance.[23] Therefore, replacing –F with O-containing groups can effectively enhance the conductivity of TMC.

The effect of treatment duration was also examined, as shown in Figure S1. The 5-min treatment resulted in the highest conductivity, followed by the 1-min treatment, while the 10-min treatment yielded the lowest conductivity. The improved conductivity

Please cite this article in press as: Silva-Quinones et al., Surface termination engineering of 2D titanium carbides for light-activated soft robotics applications, Matter (2025), https://doi.org/10.1016/j.matt.2025.102264

after short plasma treatment is attributed to modifications confined to the T_xs, converting them to O-dominated ones. With increased treatment duration, anatase TiO_2 began forming at the borders of TMC through oxidation, introducing orbital symmetry breaking of *p-d* hybridized orbitals and facilitating out-of-plane charge transfer pathways via the derived Ti–O bonds, thereby further enhancing the interfacial conductivity in TMC.[30] However, excessively prolonged treatment led to over-etching and structural distortion of the TMC, which subsequently decreases in conductivity. It is also worth noting that the 5-min treatment caused significant edge curling of the PC membrane substrate, which compromised the actuator's mechanical performance. In contrast, the 1-min treatment preserved membrane integrity while only slightly reducing conductivity. Treatments exceeding 10 min severely damaged the PC membrane. Therefore, the 1-min treatment appears to be optimal, balancing conductivity enhancement with the preservation of substrate mechanical properties.

The T_xs of TMC were characterized using X-ray photoelectron spectroscopy (XPS). In the as-fabricated TMC (see Figure S2), the Ti 2p spectra revealed four primary oxidation states, indicating the presence of Ti–C, Ti(II), Ti–O, and Ti–F bonds. The F 1s spectra showed a predominant surface F termination bonded to Ti, while the C 1s spectra exhibited peaks corresponding to C bonded to Ti and adventitious C–C bonds. This initial characterization confirmed the presence of mixed terminations, including Ti–F, Ti–OH, and Ti–O, which could adversely influence the photothermal performance of the soft actuator. After 50:50 Ar:O_2 plasma-ALE treatment, significant changes in surface composition were observed. The F 1s spectra (Figure 1C) showed that the initial TMC had a high amount of surface F bonded to Ti. After plasma-ALE treatment, a substantial decrease in F was noted, confirming the effective removal of F terminations. We observed that F termination cannot be fully replaced by O, primarily due to the limited penetration of reactive plasma species, caused by the densely stacked TMC structure[31] (see Figure S3) and structural defects[32] that hinder access to inner regions during the plasma-ALE process. Concurrently, the O 1s spectra of TMC and TMC-plasma (Figure 1D) displayed a marked increase in peaks corresponding to O–Ti and H–O–Ti bonds, indicating the successful introduction of O-containing terminations.

To further enhance the actuation performance of TMC-based soft actuators, CNFs were also incorporated to form TMC/CNF composites. The atomic percentages for TMC, TMC+CNF before and after plasma were quantified, as shown in Figure 1E. CNFs increased the C content of TMC from 45.0% to 50.4% and the O content from 18.5% to 21.8%, resulting from the cellulose composition $(C_6H_{10}O_5)_n$ and the presence of carboxylic acid groups. Plasma-ALE treatment resulted in a marked increase in O content from 21.8% to 39.9%, almost doubling the initial amount. Meanwhile, F content was reduced from 6.2% to 4.4%, confirming that the plasma-ALE process successfully converted most F-containing groups to O-containing groups. In addition, Ti content decreased from 21.6% to 15.3% and C content decreased from 50.4% to 40.0% due to the increase in new O terminations and the slight loss of Ti_3C_2 and CNFs.

Raman spectroscopy provided additional insights into the structural changes. The Raman spectra of TMC films, excited with a 785-nm laser (see Figure S4), revealed distinct regions corresponding to Ti, C, and surface groups: in-plane vibrations of surface groups attached to Ti atoms (230–470 cm^{-1}) and C vibrations (580–730 cm^{-1}).[33] After plasma treatment, the ratio between the $E_g(T_x{=}O)$ and A_{1g}(Ti, C, O) peaks—corresponding to =O T_xs and bulk vibrations, respectively—increased from 0.79 to 0.88, which is consistent with the XPS results, further confirming the effectiveness of the plasma-ALE process. To confirm that the plasma-ALE process did not induce oxidation or alter the overall structure of TMC, X-ray diffraction (XRD) analysis was performed after treatment (Figure S5). The characteristic (002) peak remained unchanged, and no peaks corresponding to TiO_2 were detected, clearly indicating that no oxidation occurred and that the structural integrity of TMC was preserved.[34]

To evaluate the long-term stability of plasma-ALE-treated TMC, samples were stored in a Petri dish under ambient conditions (~22°C, ~33% relative humidity). As shown in the O 1s spectra (Figure S6A), the intensities of O–Ti and H–O–Ti components remained nearly unchanged from 0 to 96 h, indicating that the engineered –O/–OH terminations were chemically stable. The electronic conductivity (Figure S6B) also showed minimal variation after 144 h, confirming the retention of electronic performance. These results demonstrate the long-term chemical and electronic stability of the plasma-ALE-engineered TMC under ambient conditions.

Enhancing the performance of TMC/CNF actuators

To evaluate the impact of plasma-ALE treatment on TMC/CNF actuators, we fabricated a bimorph actuator using $Ti_3C_2T_x$/cellulose composites by vacuum filtration and subsequently applied plasma-ALE to the composites. The photothermal effect of the MXene/cellulose composite was evaluated using an IR camera. The actuation mechanism of the bimorph actuator is illustrated in Figure S7. Upon exposure to NIR light, the TMC layer converts light into heat, causing water evaporation and film shrinkage, which results in actuator bending. This process is corroborated by the observed mass loss per area of the actuator during NIR irradiation, as depicted in Figure S8.

We investigated the effect of NIR light actuation on three bimorph actuators: TMC, TMC-CNF, and plasma-ALE-treated TMC-CNF (TMC-CNF-plasma), with a relative humidity of 33%. Figures 2A–2C and Videos S1–S3 show a comparison of the actuators when irradiated with NIR light for 5 s, where differences in bending angles are evident. All three actuators exhibited reversible bending behavior; among them, TMC-CNF-plasma showed the greatest degree of bending, forming a U-shape. For quantitative comparison, the bending angle versus time was measured (see Figure 2D). The maximum bending angle for TMC is 85°, which rises to 127° with the addition of CNFs. Ultimately, the TMC-CNF-plasma actuator achieves the highest maximum bending angle, 165°. These results demonstrate that plasma-enabled ALE treatment significantly enhances the light-driven actuating performance of TMC/CNF under NIR exposure. Specifically, as shown in Figure S9, the maximum temperature of the TMC-CNF-plasma composite increased to 114°C, indicating a notable improvement in photothermal conversion efficiency compared to the original material. As a control, cellulose nanofibrils deposited

Please cite this article in press as: Silva-Quinones et al., Surface termination engineering of 2D titanium carbides for light-activated soft robotics applications, Matter (2025), https://doi.org/10.1016/j.matt.2025.102264

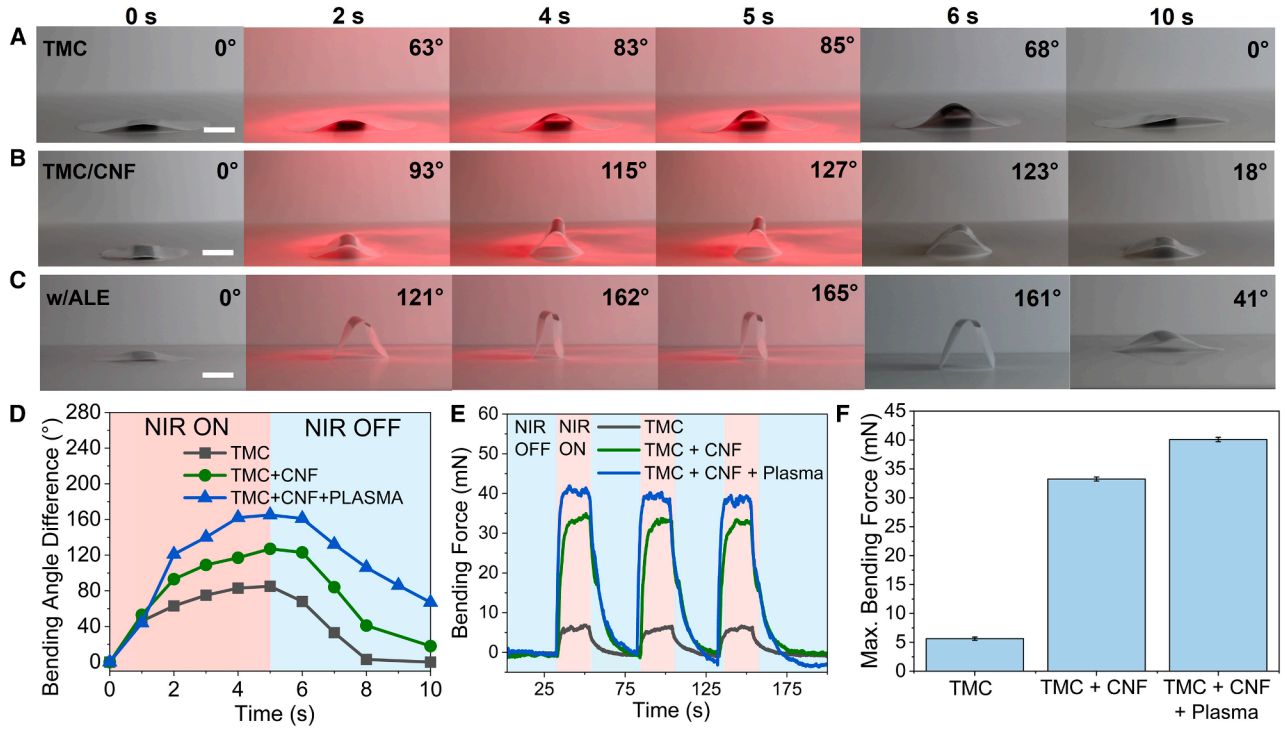

Figure 2. Light-driven performance of three bimorph TMC actuators

(A–C) Photographs of (A) TMC-only actuator, (B) TMC+CNF composite actuator, and (C) plasma-ALE-treated TMC+CNF composite actuator during one NIR on/off cycle. The scale bars in all figures are 1 cm.

(D) Bending angle versus time curves for TMC, TMC+CNF, and plasma-ALE-treated TMC-CNF actuators during one NIR on/off cycle.

(E) Bending force versus time for the TMC actuators over three NIR light on/off cycles.

(F) Maximum bending force comparison for TMC, TMC+CNF, and plasma-ALE-treated TMC-CNF actuators. Error bars represent standard error of the mean, n = 3.

on a PC membrane were also exposed to NIR light for 5 s, and no bending was observed (see Figure S10), confirming that the actuation only results from TMC photothermal activity.

Figures 2E and 2F compare the bending forces under NIR light for the three bimorph actuators. Consistent with the maximum bending angles, the maximum bending force increases from 5 mN for TMC to 33 mN for TMC-CNF and to 40 mN for TMC-CNF-plasma. The inclusion of CNFs enhances the bending force by improving the structural integrity and mechanical strength of the actuator. CNFs provide a reinforcing network that distributes stress more evenly, increasing the actuator's ability to bend and generate force in response to NIR light. The long aspect ratio of the fibrils allows for entanglement, which aids in film integrity, similar to entanglement in traditional polymer systems. Additionally, cellulose is known for its large swelling enthalpy, allowing the actuator to generate more energy and respond more efficiently to NIR irradiation.[35,36] Plasma-ALE treatment further improves the bending force by modifying the T_xs of TMC, optimizing its mechanical, electrical, and photothermal properties. The introduction of functional groups such as =O and –OH enhances the interaction between the TMC and CNF layers, resulting in improved bonding and stress transfer. Consequently, this modification increases the actuator's overall responsiveness to NIR light, leading to greater bending angles and forces. Furthermore, enhanced conductivity from plasma-enabled ALE treatment contributes to more efficient heat distribution and actuation performance. Modifying T_xs can also impact phonon dispersion, reducing phonon scattering within the MXene. This reduction enhances thermal conductivity, allowing for more effective heat dissipation and improving the overall performance of the actuators.[37]

Photothermal conversion efficiency is also a key factor influencing the light-activated actuation. As shown in Figures S11 and S12, the photothermal conversion efficiency of the pure TMC film was 40.25%, consistent with previous reports.[38] TMC-CNF showed a slightly lower efficiency (39.63%), due to reduced conductivity and free electron density after adding cellulose nanofibrils. Nevertheless, the TMC-CNF actuator exhibited enhanced NIR-driven actuation, attributed to the synergistic interaction between TMC and CNFs. TMC-CNF-plasma showed the highest efficiency (60.67%), demonstrating that plasma-ALE treatment significantly improved the photothermal performance of the TMC-CNF system.

Plasma-ALE enhancement with multiple-scale manufacturing methods

In addition to vacuum filtration, aerosol jet printing (AJP) was adopted to fabricate soft robotics at multiple scales. AJP is a contactless direct-write approach facilitating the production of fine features on a wide range of substrates.[39] Originally

Please cite this article in press as: Silva-Quinones et al., Surface termination engineering of 2D titanium carbides for light-activated soft robotics applications, Matter (2025), https://doi.org/10.1016/j.matt.2025.102264

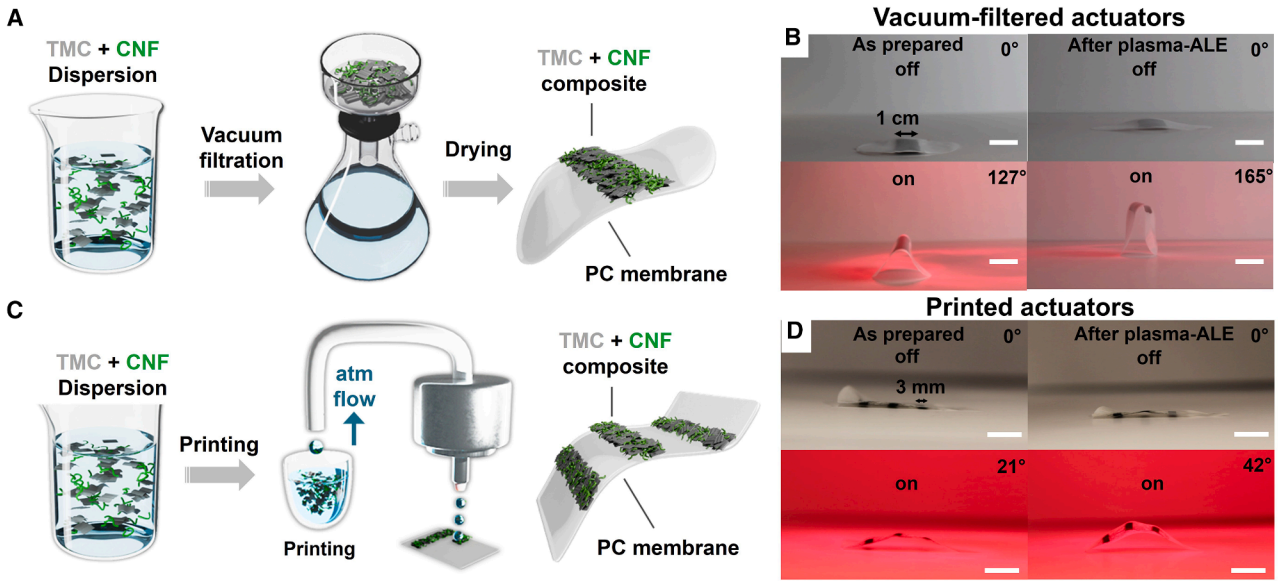

Figure 3. Plasma-ALE treated multi-scale actuators fabricated by vacuum filtration and aerosol jet printing

(A) Schematic of vacuum filtration method for centimeter-scale actuator fabrication.

(B) NIR-driven performance of vacuum-filtered actuators before and after plasma-ALE treatment.

(C) Schematic of aerosol jet printing method for millimeter-scale actuator fabrication.

(D) Demonstration of enhanced bending angle in printed actuators before and after plasma-ALE treatment under NIR light.

All scale bars in (B) and (D) images, 1 cm.

developed for electronic circuitry manufacturing, AJP has been applied in various applications such as actuators and flexible electronics,[40–42] offering desirable conformity and design flexibility.[43] As illustrated in Figures 3A and 3C, the vacuum filtration method used a vacuum to filter the water from the dispersion and cast the TMC/CNF composite onto the PC membrane, while AJP directly wrote patterns on the membrane using TMC/CNF ink. Due to their different working mechanisms, vacuum filtration enabled centimeter-scale patterning, while AJP achieved millimeter or even sub-millimeter scale features.

CNFs have two key properties that make them highly effective reinforcements in AJP inks for force-generating materials. First, the crystalline regions of cellulose exhibit an exceptionally high elastic modulus due to their unique packing density, rendering them extremely stiff.[44] Their axial modulus surpasses that of Kevlar and is comparable to highly engineered materials like carbon fibers.[45] This stiffness enables significant force generation when the material swells upon water absorption. Second, CNFs are highly hygroscopic because of abundant surface hydroxyl groups and the exponential increase in surface area at the nanoscale. Nanoscale cellulose fibers can expand in diameter by up to 45% upon water exposure.[46] This large surface area enhances reactivity with water molecules, leading to rapid and substantial swelling. Wood, known for its high swelling entropy and ability to perform significant mechanical work, exhibits swelling pressures up to 91 MPa, with theoretical maxima of 158 MPa.[44,47] As isolated forms of the stiffest and most hydrophilic component of wood, cellulose nanomaterials may achieve even higher theoretical swelling pressures and force generation. Combining CNFs with MXene ink allows light to be converted into heat, which can be used to control the water content in the material, enabling tunable actuation.

The enhancement of plasma-ALE treatment on vacuum-filtered actuators has been previously mentioned, with the maximum bending angle increasing from 127° to 165° (see Figure 3B). Leveraging the high-resolution capabilities of AJP, we designed three-strip patterns for the printed actuator, with each strip approximately 3 mm wide. Upon NIR light illumination, the printed actuator exhibited pronounced arched deformation, with the middle portion contracting the most and achieving the largest bending angle of 21° (Video S4). This angle doubled after plasma-ALE treatment (Video S5), attributed to the change from F-dominated to O-dominated T_xs and significantly enhanced light-driven performance. These findings demonstrate the versatility of plasma-ALE treatment in multi-scale actuators fabricated via different methods and dimensions, exhibiting potential as a robust solution for scalable industrial applications.

Programmable and reconfigurable soft robotics enabled by plasma-ALE treatment

Plasma-ALE treatment significantly enhances precision and efficiency in programming and reconfiguring soft robotic shapes, facilitating the realization of more complex tasks. To demonstrate this capability, we present three proof-of-concept soft robotic systems constructed with plasma-ALE-treated TMC/CNF actuators: a worm-like robot (Figure 4A; Video S6), a four-finger-like robot (Figure 4B; Video S7), and a soft gripper (Figure 4C; Video S8). NIR light serves as the stimulus to selectively heat the TMC/CNF composite, enabling dynamic and versatile shape transformations.

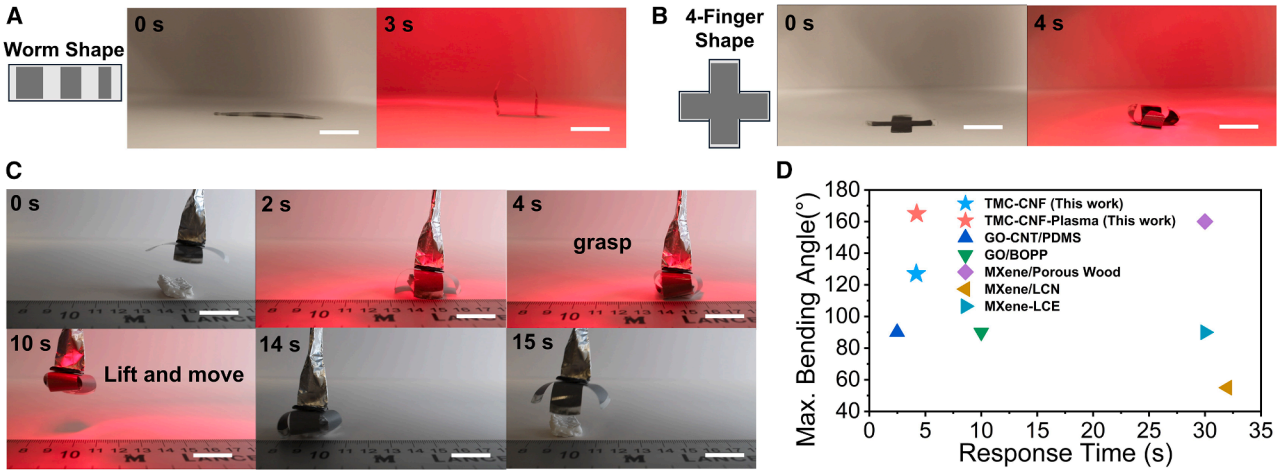

Figure 4. Soft robotic systems utilizing plasma-ALE-enhanced TMC/CNF actuators

(A) Worm-like TMC/CNF bimorph actuator and its light-driven locomotion under NIR irradiation.

(B) Four-finger TMC/CNF bimorph actuator and its response to NIR light stimulation.

(C) Gripping task demonstration using a four-finger TMC/CNF actuator.

(D) Comparison of our work with state-of-the-art 2D material-based actuators.

All scale bars, 1 cm.

The worm-like robot mimics biological movement by sequentially contracting and expanding its segments. When NIR light is applied, the strips convert heat into kinetic energy, and segments closer to the center exhibit more pronounced contraction due to variations in surface stress. All segments autonomously return to the flat state when the light is off, in a reversible and repeatable manner. Controlled directional locomotion is achieved by manipulating the incidence direction and cycles of NIR light. The four-finger-like robot serves as the foundation for a soft gripper. The fingers coated with TMC/CNF bend inward upon stimulation, and this bending behavior can be converted into gripping force. As illustrated in Figure 4C, the soft gripper is designed to delicately grasp and manipulate objects. It demonstrates practical application by lifting and moving a piece of foam weighing 4.5 times its own weight, highlighting the impressive strength-to-weight ratio of these actuators. Notably, our plasma-ALE-treated TMC/CNF soft robotics exhibit a fast response time (~4.23 s) and an ultra-large bending angle (165°), outperforming other 2D material-based actuators without plasma-ALE treatment.[12,48–51] This capability is particularly beneficial for applications in biomimetic robotics and biomedical devices like artificial muscles.[6,10] These results demonstrate that plasma-ALE-treated TMC/CNF actuators enable the fabrication of intricate and multifunctional structures in soft robotics.

DISCUSSION

This study demonstrates the effectiveness of plasma-ALE in engineering the T_xs of TMC, significantly enhancing its conductivity and photothermal properties for stimuli-responsive materials. By optimizing the O_2:Ar ratio, plasma-ALE treatment effectively removes fluorine (–F) terminations and introduces oxygen (–O) and hydroxyl (–OH) groups. This modification results in an 80% increase in electrical conductivity and a dramatic improvement in photothermal actuation performance. Integration with CNFs further amplifies actuator capabilities, achieving a 165° bending angle and a 40 mN bending force under NIR light illumination after plasma-ALE treatment. The compatibility of the plasma-ALE process was validated across multiple manufacturing methods, including vacuum filtration and AJP, highlighting its versatility and potential for large-scale fabrication. Additionally, ALE-modified TMC/CNF enables the development of programmable and reconfigurable soft robotic structures, such as soft grippers and worm-like robots. These advancements showcase the potential for advanced applications in biomedical devices, flexible electronics, and environmental monitoring systems. This work provides a robust framework for the surface engineering of TMC, illustrating the potential of ALE-based modifications to drive the development of next-generation multifunctional materials and high-performance soft robotics applications.

METHODS

Synthesis of TMC nanosheets

TMC nanosheets were synthesized and delaminated using the MILD method, which employs a LiF/HCl mixture to generate *in situ* hydrofluoric acid (HF). To prepare the etching solution, 40 mL 9 M HCl was mixed with 2 g LiF in a polytetrafluoroethylene container and agitated with a magnetic stir bar for 30 min at room temperature. Subsequently, 2 g Ti_3AlC_2 powder (MAX Phase, ≥90%; Sigma-Aldrich) was gradually added to the etching solution. The etching process was maintained for 48 h under magnetic stirring at 35°C. Following etching, the reaction products were washed with deionized water and centrifuged at 4,000 rpm for 8 min over several cycles until the pH exceeded 6. The resulting sediment was then subjected to sonication in

Please cite this article in press as: Silva-Quinones et al., Surface termination engineering of 2D titanium carbides for light-activated soft robotics applications, Matter (2025), https://doi.org/10.1016/j.matt.2025.102264

an ice water bath for 2 h to delaminate multilayers into single-layer TMC (see Figure S13). The dispersion was subsequently centrifuged at 3,500 rpm for 1 h to sediment any MAX or unexfoliated $Ti_3C_2T_x$ sheets. Finally, the TMC nanosheet solution was collected from the supernatant and stored at 4°C to prevent oxidation.

Synthesis of TMC-CNF composite

TMC was composited with cellulose nanofibrils to form the actuation material system. The cellulose nanofibrils used were derived from paper pulp (from trees) using a mechanical refining process: pulp fibers were passed through disk refiners until the elementary fibrils of the tree's structure were separated.[52] There are several ways to produce cellulose nanomaterials, but mechanical refinement appears to be the most cost-effective. The elementary structural fibrils of trees are typically 10 nm in diameter (varies depending on species type) and consist of high-aspect-ratio crystalline regions connected by amorphous regions to form long continuous fibers.[45] Cellulose nanomaterials from trees are widely studied because paper pulp (which is isolated cellulose) is a well-established industrial commodity that serves as a good source for further processing down to the nanoscale. The TMC-CNF mixture was prepared by combining TMC nanosheets with CNFs and subjecting the mixture to bath sonication for 1 h. The TMC-to-cellulose weight ratio in the solution was maintained at 10:1, and the concentration of the TMC-CNF mixture was set at 0.5 wt %. The resulting solution was then stored at 4°C.

Fabrication of the TMC-CNF/PC bilayer actuator

The TMC-CNF/PC bilayer-structured actuator was fabricated by vacuum filtering the TMC-CNF solution onto a PC filter membrane (Millipore, GTTP04700). A mask was employed during the filtering process to pattern the actuator. Similarly, TMC/PC bilayer-structured actuators were prepared on the same PC filter membrane for comparison. The actuators were then left to dry in air for 2 h.

AJP of TMC-CNF/PC bilayer actuator

Micron-scale printer paths were designed using AutoCAD software. The atomizer and sheath flow pressures were allowed to stabilize before printing. All patterns were printed at room temperature using a 150-μm diameter nozzle at a print speed of 2 mm/s. The sheath flow rate was maintained between 20 and 25 sccm, the atomizer flow rate was set between 20 and 28 sccm, and the applied ultrasonic inducer current was set at 500 mA.

Plasma treatment of the TMC-CNF/PC bilayer actuator

Once the actuators were dry, they were transferred to a plasma asher (Glow Research, AutoGlow 200) in the cleanroom for plasma-enabled ALE treatment. The actuators were secured by clipping them to an Si wafer. Various plasma conditions were tested by adjusting the O_2:Ar ratios to 0%, 20%, 50%, 80%, and 100%, while maintaining a constant power of 100 W and a duration of 1 min. Immediately after plasma treatment, the samples were subjected to conductivity measurements using a four-point probe method (source current: 0.01 A, geometrical correction factor: 4.2076).

Characterization

The characterization of MXene, cellulose, and their composites was carried out using a range of material characterization techniques. XPS was performed using a Kratos instrument equipped with an Al Kα source to analyze surface functional groups. XRD was conducted with an Anton Paar XRDynamic 500 equipped with a Cu X-ray source to assess crystalline structure. Morphological features were examined using scanning electron microscopy (Thermo Fisher Scientific, Apreo S). Raman spectroscopy was conducted with a Horiba Jobin Yvon LabRAM ARAMIS to investigate vibrational modes. Surface topography was analyzed using an Asylum Research Jupiter XR atomic force microscope. The bending force of the actuators in response to NIR light was measured using a TA Instruments RSA-G2 Solids Analyzer. NIR irradiation was provided by a 660-W RubyLux lamp with a wavelength of 850 nm.

Photothermal conversion efficiency

The photothermal conversion efficiency (η) was calculated using Equation 1[38,53]:

$$\eta = \frac{hS(T_m - T_s)}{P}, \qquad \text{(Equation 1)}$$

where h is the heat transfer coefficient; S is the surface area of the system; T_m and T_s are the maximum steady-state and ambient temperatures, respectively; and P is the power of the incident light. The product hS was determined from the linear fitting of cooling period data using the following relationships:

$$t = \frac{\sum_i m_i C_{p,i}}{hS} 1n\theta \qquad \text{(Equation 2)}$$

$$\theta = \frac{T - T_s}{T_m - T_s} \qquad \text{(Equation 3)}$$

where m_i and $c_{p,i}$ are the mass and specific heat capacity of each component in the system. The heat capacity and cooling data for photothermal conversion calculations were obtained using a differential scanning calorimeter (DSC 2500, TA Instruments) and an 808-nm continuous-wave laser with adjustable power (CivilLaser).

RESOURCE AVAILABILITY

Lead contact

Further information and requests for resources and materials should be directed to and will be fulfilled by the lead contact, Haozhe Wang (haozhe.wang@duke.edu).

Materials availability

All unique materials generated in this study are available from the lead contact with a completed materials transfer agreement.

Data and code availability

All the raw data are available online at Harvard Dataverse (https://doi.org/10.7910/DVN/XQ6MY8). The study did not generate any code.

ACKNOWLEDGMENTS

The authors gratefully acknowledge the support from the P3Nano program of the Forest Products Laboratory (USDA Forest Service Agreement No. 24-JV-11111124-078). This material is based upon work supported by the National Science Foundation under award no. 2443257. We also thank P. Yao, M.D. Walters, and R. Garces for their assistance with MXene synthesis, characterization, and DSC measurements. This work was performed in part at the Duke University Shared Materials Instrumentation Facility, a member of the North Carolina Research Triangle Nanotechnology Network, which is supported by the National Science Foundation (award no. ECCS-2025064) as part of the National Nanotechnology Coordinated Infrastructure.

AUTHOR CONTRIBUTIONS

H.W. conceived the original idea and supervised the overall project. D.S.-Q., X.H., and H.W. performed the materials synthesis, plasma treatment, and materials characterization. B.C., A.B., and A.D.F. conducted the AJP experiments. D.S.-Q., X.H., A.H., Y.Z., and H.W. synthesized TMC/CNF actuators and characterized their actuation performance. W.C. drafted schematics illustrating the multi-scale manufacturing methods. X.H., W.B., and H.W. performed the analysis of the mechanisms of conductivity enhancement in plasma-ALE-treated TMC. Q.Y. and D.F. synthesized the CNFs. D.S.-Q, X.H., J.W., and H.W. performed the XPS characterization and its analysis. M.D.D. performed the analysis of actuation mechanism. D.S.-Q., X.H., and H.W. drafted the manuscript. All authors reviewed and revised the manuscript.

DECLARATION OF INTERESTS

The authors declare no competing interests.

SUPPLEMENTAL INFORMATION

Supplemental information can be found online at https://doi.org/10.1016/j.matt.2025.102264.

Received: October 29, 2024
Revised: April 23, 2025
Accepted: June 9, 2025

REFERENCES

1. Zeng, S., Ye, Y., Zhou, P., Yi, S., Guo, Q., Chen, H., Shen, G., and Weng, M. (2024). Programmable and reconfigurable humidity-driven actuators made with MXene (Ti3C2Tx)-cellulose nanofiber composites for biomimetic applications. Nano Res. *17*, 6619–6629. https://doi.org/10.1007/s12274-024-6542-4.
2. Mano, J.F. (2008). Stimuli-responsive polymeric systems for biomedical applications. Adv. Eng. Mater. *10*, 515–527. https://doi.org/10.1002/adem.200700355.
3. Nguyen, V.H., Tabassian, R., Oh, S., Nam, S., Mahato, M., Thangasamy, P., Rajabi-Abhari, A., Hwang, W.J., Taseer, A.K., and Oh, I.K. (2020). Stimuli-Responsive MXene-Based Actuators. Adv. Funct. Mater. *30*, 1909504. https://doi.org/10.1002/adfm.201909504.
4. Gao, J., Tang, Y., Martella, D., Guo, J., Wiersma, D.S., and Li, Q. (2023). Stimuli-responsive photonic actuators for integrated biomimetic and intelligent systems. Responsive Materials *1*, e20230008. https://doi.org/10.1002/rpm.20230008.
5. Liu, Y., Genzer, J., and Dickey, M.D. (2016). "2D or not 2D": Shape-programming polymer sheets. Prog. Polym. Sci. *52*, 79–106. https://doi.org/10.1016/j.progpolymsci.2015.09.001.
6. Shen, Z., Chen, F., Zhu, X., Yong, K.T., and Gu, G. (2020). Stimuli-responsive functional materials for soft robotics. J. Mater. Chem. B *39*, 8972–8991. https://doi.org/10.1039/d0tb01585g.
7. Zhang, Q., Zhang, J., Wan, S., Wang, W., and Fu, L. (2018). Stimuli-Responsive 2D Materials Beyond Graphene. Adv. Funct. Mater. *28*, 1802500. https://doi.org/10.1002/adfm.201802500.
8. Wang, J., Cai, Z., Lin, D., Chen, K., Zhao, L., Xie, F., Su, R., Xie, W., Liu, P., and Zhu, R. (2021). Plasma Oxidized Ti3C2Tx MXene as Electron Transport Layer for Efficient Perovskite Solar Cells. ACS Appl. Mater. Interfaces *13*, 32495–32502. https://doi.org/10.1021/acsami.1c07146.
9. Lin, H., Wang, X., Yu, L., Chen, Y., and Shi, J. (2017). Two-Dimensional Ultrathin MXene Ceramic Nanosheets for Photothermal Conversion. Nano Lett. *17*, 384–391. https://doi.org/10.1021/acs.nanolett.6b04339.
10. Cai, G., Ciou, J.-H., Liu, Y., Jiang, Y., and Lee, P.S. (2019). Leaf-inspired multiresponsive MXene-based actuator for programmable smart devices. Sci. Adv. *5*, eaaw7956. https://doi.org/10.1126/sciadv.aaw7956.
11. Iravani, S. (2023). Role of MXenes in advancing soft robotics. Soft Matter *19*, 6196–6212. https://doi.org/10.1039/d3sm00756a.
12. Ge, S., Yin, S., Li, X., Zhao, Y., Ma, H., and Sun, Y. (2023). Near-infrared photo-responsive Ti3C2Tx MXene/LCN film for soft actuators. Liq. Cryst. *50*, 2529–2539. https://doi.org/10.1080/02678292.2023.2264252.
13. Zhao, T., Liu, H., Yuan, L., Tian, X., Xue, X., Li, T., Yin, L., and Zhang, J. (2022). A Multi-Responsive MXene-Based Actuator with Integrated Sensing Function. Adv. Mater. Interfaces *9*, 2101948. https://doi.org/10.1002/admi.202101948.
14. Adomaviciute-Grabusove, S., Popov, A., Ramanavicius, S., Sablinskas, V., Shevchuk, K., Gogotsi, O., Baginskiy, I., Gogotsi, Y., and Ramanavicius, A. (2024). Monitoring Ti3C2Tx MXene Degradation Pathways Using Raman Spectroscopy. ACS Nano *18*, 13184–13195. https://doi.org/10.1021/acsnano.4c02150.
15. Alhabeb, M., Maleski, K., Anasori, B., Lelyukh, P., Clark, L., Sin, S., and Gogotsi, Y. (2017). Guidelines for Synthesis and Processing of Two-Dimensional Titanium Carbide (Ti3C2Tx MXene). Chem. Mater. *29*, 7633–7644. https://doi.org/10.1021/acs.chemmater.7b02847.
16. Miao, B., Bashir, T., Zhang, H., Ali, T., Raza, S., He, D., Liu, Y., and Bai, J. (2024). Impact of various 2D MXene surface terminating groups in energy conversion. Renew. Sustain. Energy Rev. *199*, 114506. https://doi.org/10.1016/j.rser.2024.114506.
17. Bark, H., Thangavel, G., Liu, R.J., Chua, D.H.C., and Lee, P.S. (2023). Effective surface modification of 2D MXene toward thermal energy conversion and management. Small Methods *7*, 2300077. https://doi.org/10.1002/smtd.202300077.
18. Halim, J., Persson, I., Eklund, P., Persson, P.O.Å., and Rosen, J. (2018). Sodium hydroxide and vacuum annealing modifications of the surface terminations of a Ti3C2 (MXene) epitaxial thin film. RSC Adv. *8*, 36785–36790. https://doi.org/10.1039/C8RA07270A.
19. Tang, H., Wang, R., Shi, L., Sheremet, E., Rodriguez, R.D., and Sun, J. (2021). Post-processing strategies for improving the electrical and mechanical properties of MXenes. Chem. Eng. J. *425*, 131472. https://doi.org/10.1016/j.cej.2021.131472.
20. Bao, Z., Lu, C., Cao, X., Zhang, P., Yang, L., Zhang, H., Sha, D., He, W., Zhang, W., Pan, L., and Sun, Z. (2021). Role of MXene surface terminations in electrochemical energy storage: a review. Chin. Chem. Lett. *32*, 2648–2658. https://doi.org/10.1016/j.cclet.2021.02.012.
21. Zou, J., Wu, J., Wang, Y., Deng, F., Jiang, J., Zhang, Y., Liu, S., Li, N., Zhang, H., Yu, J., et al. (2022). Additive-mediated intercalation and surface modification of MXenes. Chem. Soc. Rev. *51*, 2972–2990. https://doi.org/10.1039/D0CS01487G.
22. Xu, W., Li, S., Zhang, W., Ouyang, B., Yu, W., and Zhou, Y. (2021). Nitrogen-Doped Ti3C2Tx MXene Induced by Plasma Treatment with Enhanced Microwave Absorption Properties. ACS Appl. Mater. Interfaces *13*, 49242–49253. https://doi.org/10.1021/acsami.1c17015.

23. Liu, P., Ding, W., Liu, J., Shen, L., Jiang, F., Liu, P., Zhu, Z., Zhang, G., Liu, C., and Xu, J. (2020). Surface termination modification on high-conductivity MXene film for energy conversion. J. Alloys Compd. *829*, 154634. https://doi.org/10.1016/j.jallcom.2020.154634.

24. Khanal, R., and Irle, S. (2023). Effect of surface functional groups on MXene conductivity. J. Chem. Phys. *158*, 194701. https://doi.org/10.1063/5.0141589.

25. Guo, L., Wang, X., Leong, Z.Y., Mo, R., Sun, L., and Yang, H.Y. (2018). Ar plasma modification of 2D MXene Ti3C2Tx nanosheets for efficient capacitive desalination. FlatChem *8*, 17–24. https://doi.org/10.1016/j.flatc.2018.01.001.

26. Hegemann, D., Brunner, H., and Oehr, C. (2003). Plasma treatment of polymers for surface and adhesion improvement. Nuclear instruments and methods in physics research section B: Beam interactions with materials and atoms *208*, 281–286. https://doi.org/10.1016/S0168-583X(03)00644-X.

27. Jung, H., Oh, I.K., Yoon, C.M., Park, B.E., Lee, S., Kwon, O., Lee, W.J., Kwon, S.H., Kim, W.H., and Kim, H. (2018). Effects of Ar Addition to O2 Plasma on Plasma-Enhanced Atomic Layer Deposition of Oxide Thin Films. ACS Appl. Mater. Interfaces *10*, 40286–40293. https://doi.org/10.1021/acsami.8b14244.

28. Zhang, W., Ji, X.-X., and Ma, M.-G. (2023). Emerging MXene/cellulose composites: Design strategies and diverse applications. Chem. Eng. J. *458*, 141402. https://doi.org/10.1016/j.cej.2023.141402.

29. Schultz, T., Frey, N.C., Hantanasirisakul, K., Park, S., May, S.J., Shenoy, V.B., Gogotsi, Y., and Koch, N. (2019). Surface termination dependent work function and electronic properties of Ti3C2Tx MXene. Chem. Mater. *31*, 6590–6597. https://doi.org/10.1021/acs.chemmater.9b00414.

30. Wu, Y., Li, Y., Liu, Y., Zhu, D., Xing, S., Lambert, N., Weisbecker, H., Liu, S., Davis, B., Zhang, L., et al. (2024). Orbit symmetry breaking in MXene implements enhanced soft bioelectronic implants. Sci. Adv. *10*, eadp8866. https://doi.org/10.1126/sciadv.adp8866.

31. Shi, X., Yu, Z., Liu, Z., Cao, N., Zhu, L., Liu, Y., Zhao, K., Shi, T., Yin, L., and Fan, Z. (2025). Scalable, High-Yield Monolayer MXene Preparation from Multilayer MXene for Many Applications. Angew. Chem. *64*, e202418420. https://doi.org/10.1002/ange.202418420.

32. Ravi Kumar, Y., Deshmukh, K., Mohamed Naseer Ali, M., Rajabathar, J.R., Theerthagiri, J., Pandey, M., and Pasha, S.K.K. (2022). Structure defects and electronic properties of MXenes. Mxenes and their Composites, 91–129. https://doi.org/10.1016/B978-0-12-823361-0.00005-8.

33. Sarycheva, A., and Gogotsi, Y. (2023). Raman Spectroscopy Analysis of the Structure and Surface Chemistry of Ti3C2Tx MXene (Jenny Stanford Publishing), pp. 333–355.

34. Li, Z., Wang, L., Sun, D., Zhang, Y., Liu, B., Hu, Q., and Zhou, A. (2015). Synthesis and thermal stability of two-dimensional carbide MXene Ti3C2. Mater. Sci. Eng., B *191*, 33–40. https://doi.org/10.1016/j.mseb.2014.10.009.

35. Faisal, M., Žmirić, M., Kim, N., Bruun, S., Mariniello, L., Famiglietti, M., Bordallo, H., Kirkensgaard, J., Jørgensen, B., Ulvskov, P., et al. (2023). A Comparison of Cellulose Nanocrystals and Nanofibers as Reinforcements to Amylose-Based Composite Bioplastics. Coatings *13*, 1573. https://doi.org/10.3390/coatings13091573.

36. Xu, X., Liu, F., Jiang, L., Zhu, J.Y., Haagenson, D., and Wiesenborn, D.P. (2013). Cellulose nanocrystals vs. cellulose nanofibrils: a comparative study on their microstructures and effects as polymer reinforcing agents. ACS Appl. Mater. Interfaces *5*, 2999–3009. https://doi.org/10.1021/am302624t.

37. Wang, M., Liu, Y., Zhang, H., Wu, Y., and Pan, L. (2022). Thermal conductivities of Ti3C2Tx MXenes and their interfacial thermal performance in MXene/epoxy composites–a molecular dynamics simulation. Int. J. Heat Mass Tran. *194*, 123027. https://doi.org/10.1016/j.ijheatmasstransfer.2022.123027.

38. Shin, H., Jeong, W., and Han, T.H. (2024). Maximizing light-to-heat conversion of Ti3C2Tx MXene metamaterials with wrinkled surfaces for artificial actuators. Nat. Commun. *15*, 10507. https://doi.org/10.1038/s41467-024-54802-0.

39. Secor, E.B. (2018). Principles of aerosol jet printing. Flex. Print. Electron. *3*, 035002. https://doi.org/10.1088/2058-8585/aace28.

40. Zhang, B., Hobbie, H.A., Wu, Y., Bai, W., and Franklin, A.D. (2024). MXene-contacted Carbon Nanotube Thin-Film Transistors using Aerosol Jet Printing. IEEE Trans. Mat. Electron Devices *1*, 90–96. https://doi.org/10.1109/TMAT.2024.3443753.

41. Lu, S., Smith, B.N., Meikle, H., Therien, M.J., and Franklin, A.D. (2023). All-carbon thin-film transistors using water-only printing. Nano Lett. *23*, 2100–2106. https://doi.org/10.1021/acs.nanolett.2c04196.

42. Williams, N.X., Bullard, G., Brooke, N., Therien, M.J., and Franklin, A.D. (2021). Printable and recyclable carbon electronics using crystalline nanocellulose dielectrics. Nat. Electron. *4*, 261–268. https://doi.org/10.1038/s41928-021-00574-0.

43. Wilkinson, N.J., Smith, M.A.A., Kay, R.W., and Harris, R.A. (2019). A review of aerosol jet printing—a non-traditional hybrid process for micro-manufacturing. Int. J. Adv. Manuf. Technol. *105*, 4599–4619. https://doi.org/10.1007/s00170-019-03438-2.

44. Nishiyama, Y. (2023). Thermodynamics of the swelling work of wood and non-ionic polysaccharides: a revisit. Carbohydr. Polym. *320*, 121227. https://doi.org/10.1016/j.carbpol.2023.121227.

45. Moon, R.J., Martini, A., Nairn, J., Simonsen, J., and Youngblood, J. (2011). Cellulose nanomaterials review: structure, properties and nanocomposites. Chem. Soc. Rev. *40*, 3941–3994. https://doi.org/10.1039/C0CS00108B.

46. Ottesen, V., and Syverud, K. (2021). Swelling of individual cellulose nanofibrils in water, role of crystallinity: an AFM study. Cellulose *28*, 19–29. https://doi.org/10.1007/s10570-020-03517-8.

47. Tarkow, H., and Turner, H. (1958). The Swelling Pressure of Wood, *8*, pp. 193–196.

48. Yang, M., Xu, Y., Zhang, X., Bisoyi, H.K., Xue, P., Yang, Y., Yang, X., Valenzuela, C., Chen, Y., Wang, L., et al. (2022). Bioinspired phototropic MXene-reinforced soft tubular actuators for omnidirectional light-tracking and adaptive photovoltaics. Adv. Funct. Mater. *32*, 2201884. https://doi.org/10.1002/adfm.202201884.

49. Zhang, D., Yang, K., Liu, X., Luo, M., Li, Z., Liu, C., Li, M., Chen, W., and Zhou, X. (2022). Boosting the photothermal conversion efficiency of MXene film by porous wood for Light-driven soft actuators. Chem. Eng. J. *450*, 138013. https://doi.org/10.1016/j.cej.2022.138013.

50. Wang, W., Xiang, C., Zhu, Q., Zhong, W., Li, M., Yan, K., and Wang, D. (2018). Multistimulus responsive actuator with GO and carbon nanotube/PDMS bilayer structure for flexible and smart devices. ACS Appl. Mater. Interfaces *10*, 27215–27223. https://doi.org/10.1021/acsami.8b08554.

51. Chen, L., Weng, M., Zhou, P., Zhang, L., Huang, Z., and Zhang, W. (2017). Multi-responsive actuators based on a graphene oxide composite: intelligent robot and bioinspired applications. Nanoscale *9*, 9825–9833. https://doi.org/10.1039/C7NR01913K.

52. Kelly, P.V., Gardner, D.J., and Gramlich, W.M. (2021). Optimizing lignocellulosic nanofibril dimensions and morphology by mechanical refining for enhanced adhesion. Carbohydr. Polym. *273*, 118566. https://doi.org/10.1016/j.carbpol.2021.118566.

53. Cao, Y., Dou, J.-H., Zhao, N.-j., Zhang, S., Zheng, Y.-Q., Zhang, J.-P., Wang, J.-Y., Pei, J., and Wang, Y. (2017). Highly efficient NIR-II photothermal conversion based on an organic conjugated polymer. Chem. Mater. *29*, 718–725. https://doi.org/10.1021/acs.chemmater.6b04405.

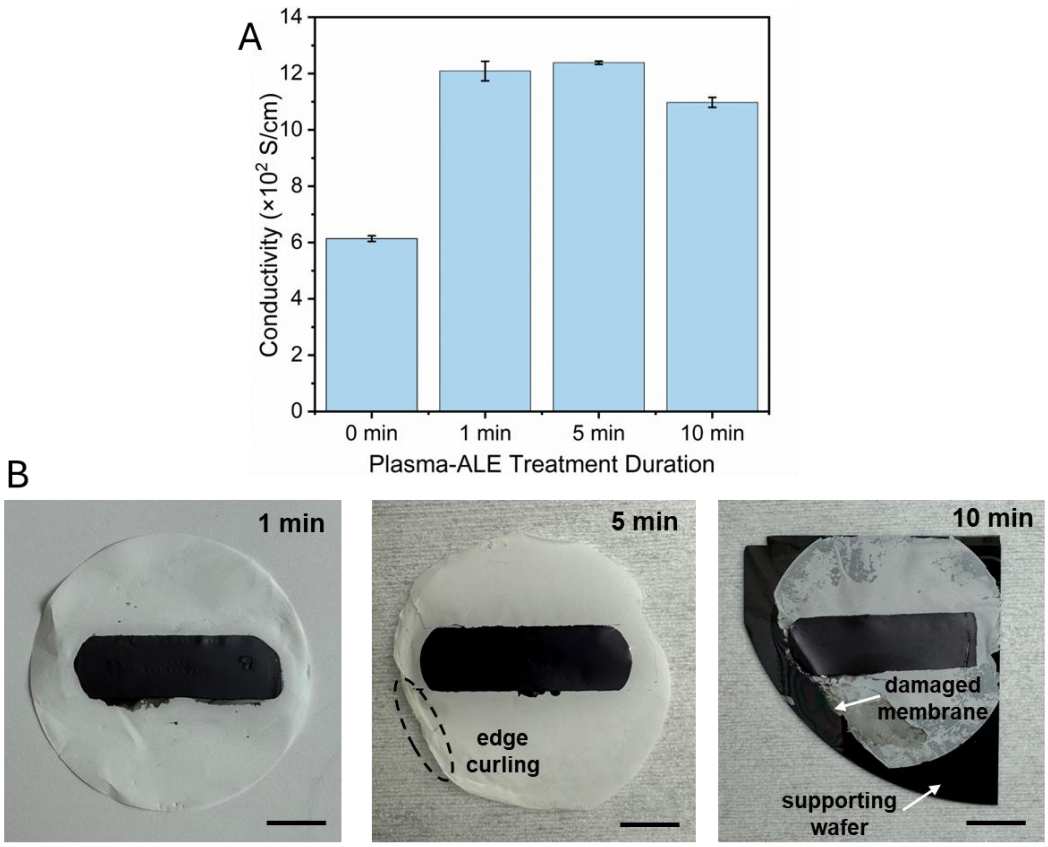

Figure S1. Effects of plasma-ALE treatment duration on (a) electrical conductivity and (b) PC membrane substrates of TMC films.

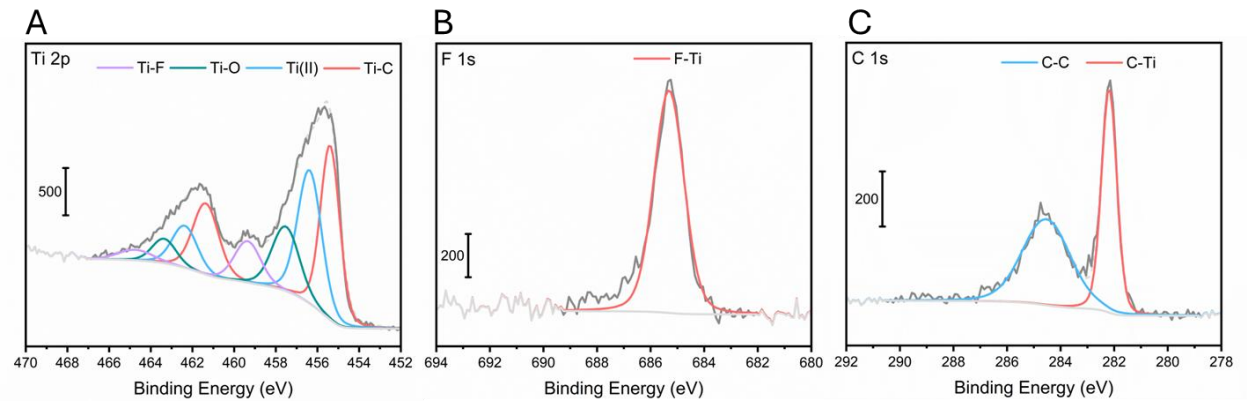

Figure S2. XPS analysis of the as-synthesized TMC surface chemistry. High-resolution XPS spectra of (a) Ti 2p, (b) F 1s, and (c) C 1s regions.

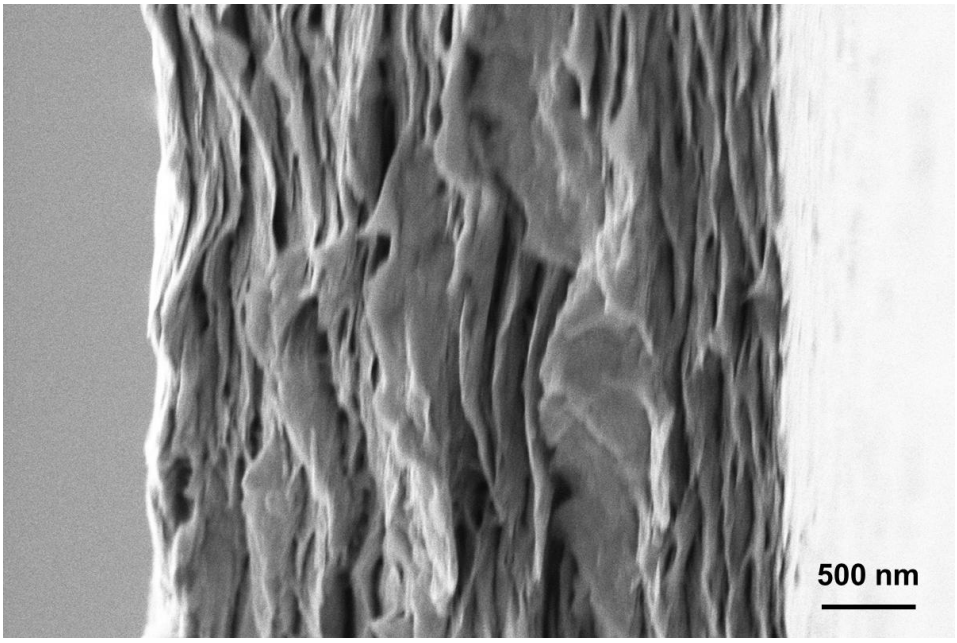

Figure S3. SEM image of densely stacked TMC multilayers.

A

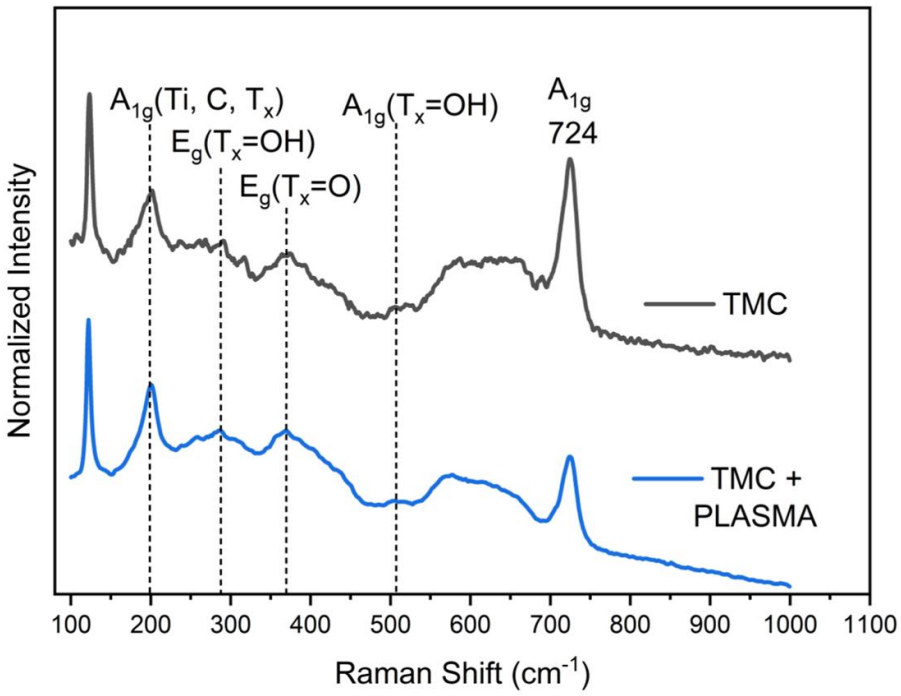

B

Sample	Eg (Tx=O) / A1g (Ti, C, O)
TMC	0.79
TMC-PLASMA	0.88

Figure S4. Comparison of Raman spectra of TMC-based films. (a) From top to bottom: as-synthesized TMC film, and plasma-ALE-treated TMC film. (b) Calculated ratios of A_{1g}(Ti, C, O) and $E_g(T_x{=}O)$ peaks.

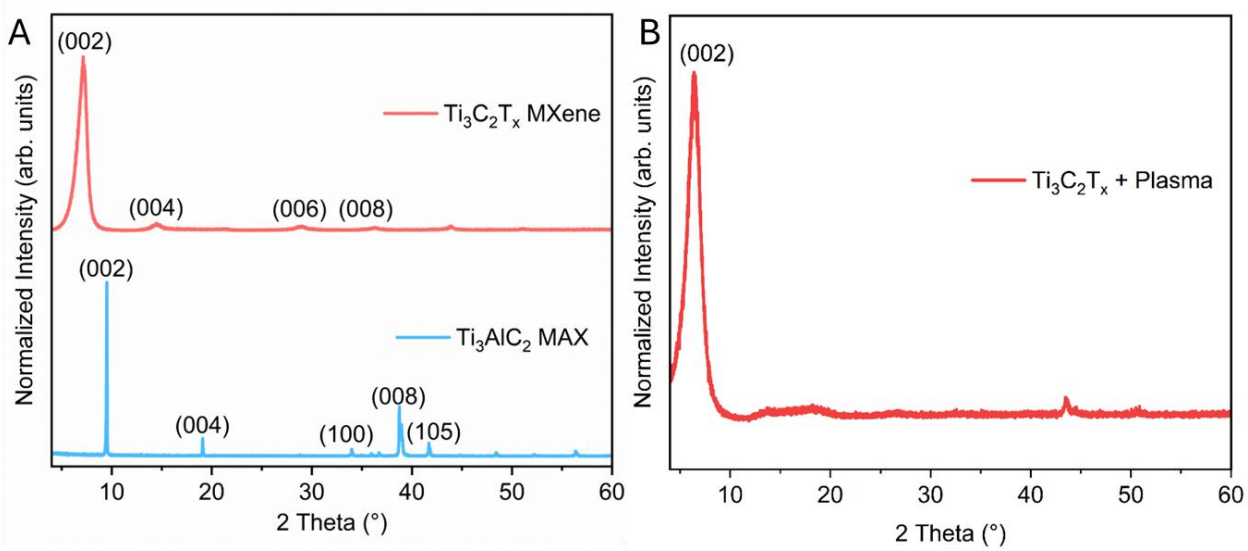

Figure S5. XRD spectra of (a) MILD-synthesized $Ti_3C_2T_x$ and Ti_3AlC_2 powder precursor, (b) $Ti_3C_2T_x$ after plasma-ALE treatment.

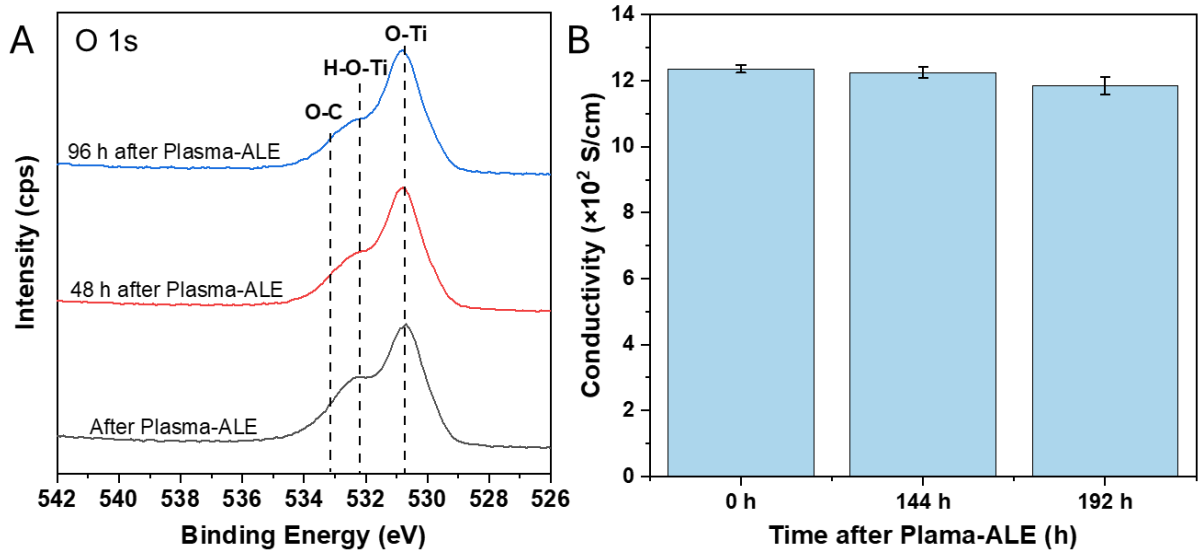

Figure S6. Stability of plasma-ALE-treated TMC. (a) High-resolution O 1s XPS spectra collected at 0, 48, and 96 h after treatment. (b) Electrical conductivity measured at 0, 144, and 192 h after treatment.

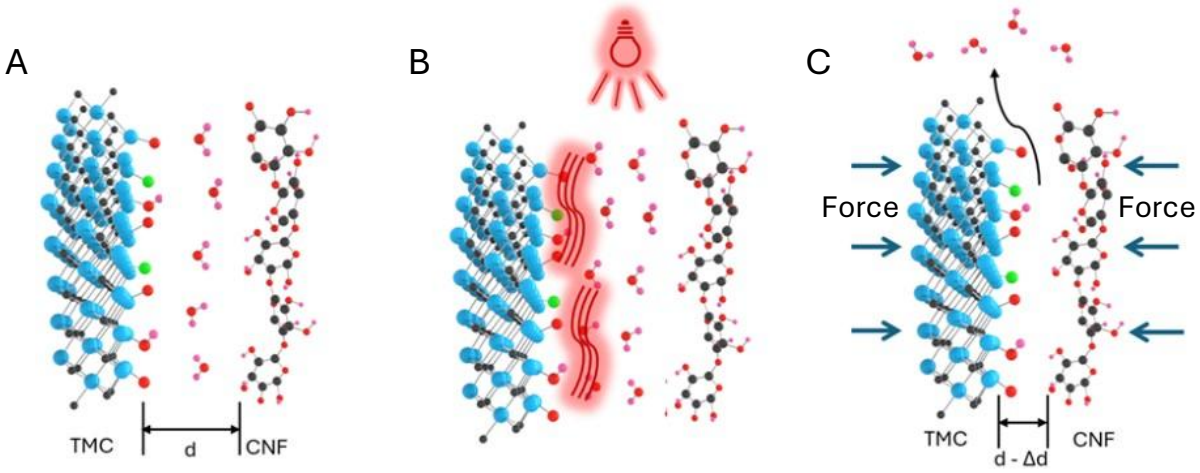

Figure S7. Schematic illustration of light-driven actuation process in TMC-CNF composites. (a) Initial state of the TMC/CNF composite, with water absorbed at the TMC-CNF interface. (b) Under IR light irradiation, TMC exhibits a photothermal effect, converting photons into phonons and generating heat. (c) The absorbed water evaporates, producing compressive forces that drive the actuation of the composite.

A

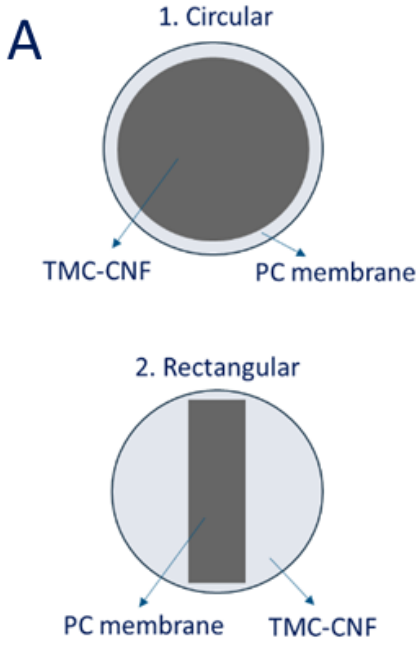

B

Sample	Mass loss per area (mg/cm^2)
1. Circular	0.067 ± 0.03
2. Rectangular	0.119 ± 0.07

Figure S8. Mass loss per area of TMC/CNF composite films after 60-second NIR light irradiation. Measurements were conducted on both circular and rectangular film samples, all prepared by vacuum filtration.

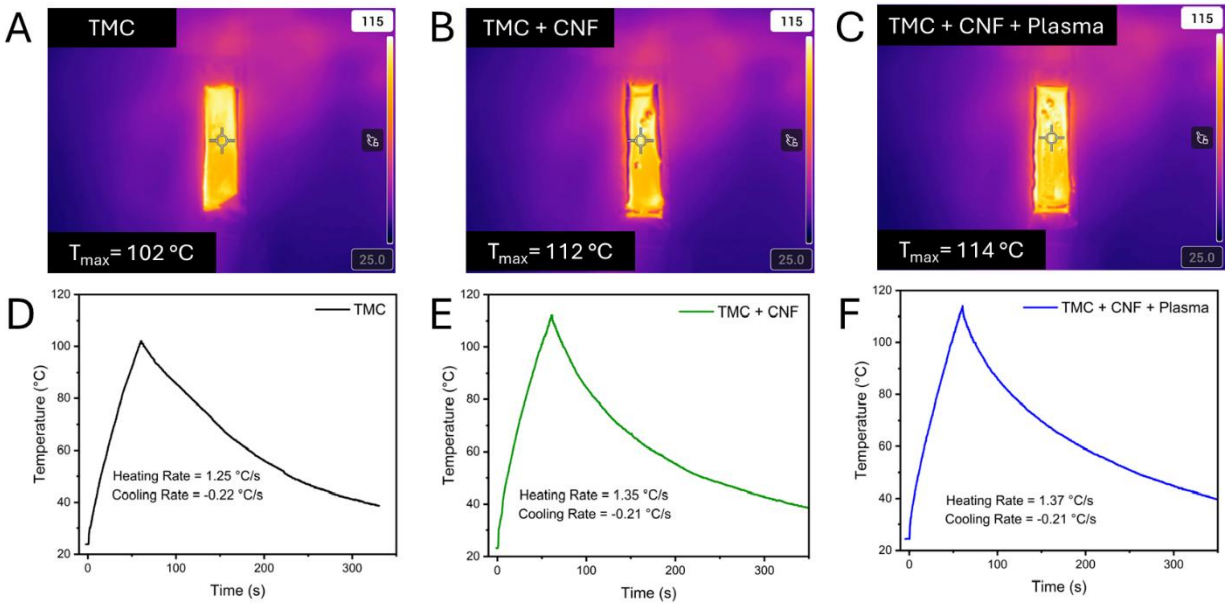

Figure S9. Thermal analysis of TMC-based samples under NIR light irradiation. Thermal images of (a) original TMC, (b) TMC-CNF composite, and (c) plasma ALE-treated TMC-CNF composite, after 1 minute of NIR exposure. Temperature curves for (d) original TMC, (e) TMC-CNF composite, and (f) plasma ALE-treated TMC-CNF composite.

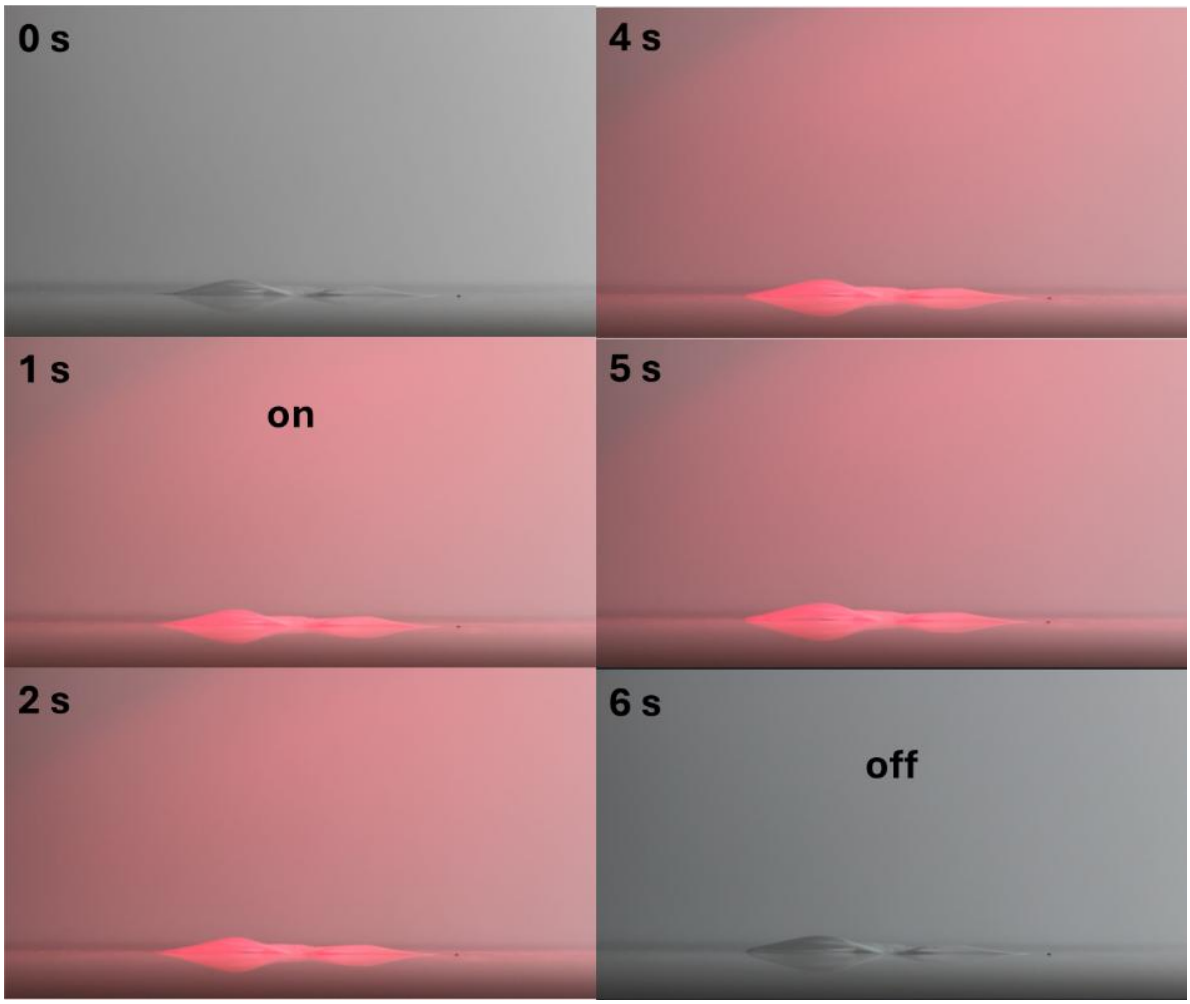

Figure S10. Photothermal response test of pure Cellulose Nanofibrils (CNFs). CNF film deposited on a polycarbonate (PC) membrane and exposed to NIR light for 5 seconds, demonstrating the absence of photothermal actuation without TMC.

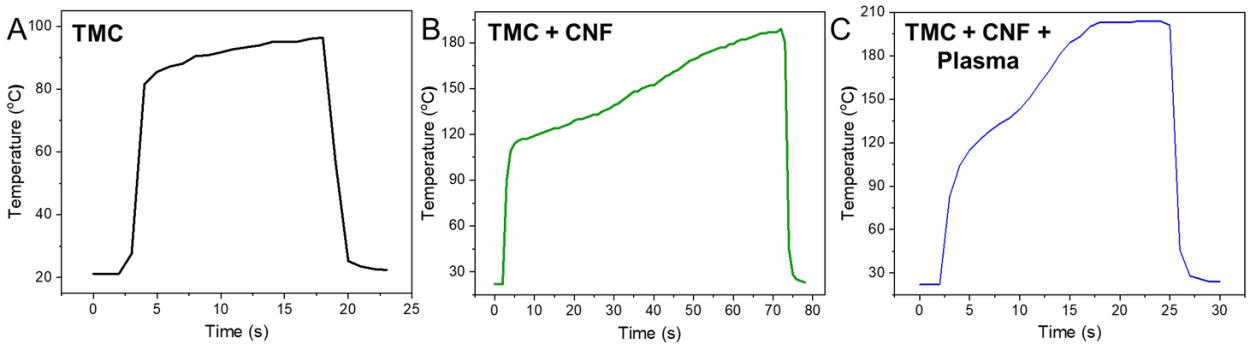

Figure S11. Temperature profiles of (a) TMC, (b) TMC-CNF composite, and (c) plasma-ALE-treated TMC-CNF composite under 808 nm laser irradiation.

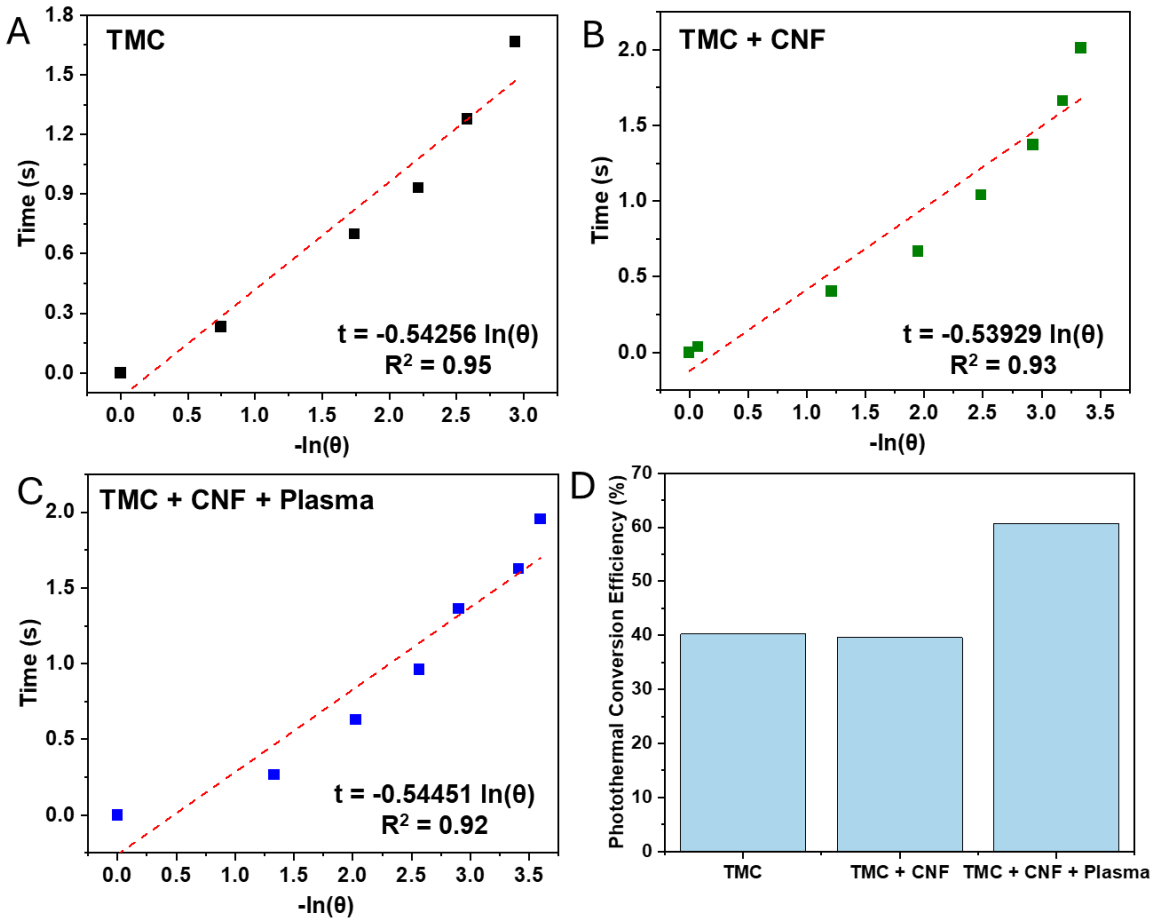

Figure S12. Results of photothermal conversion efficiency calculation. Linear fitting of the cooling period between cooling time and -lnθ for (a) TMC, (b) TMC + CNF, and (c) TMC + CNF + Plasma; (d) photothermal conversion efficiencies of TMC, TMC+CNF, TMC+CNF+Plasma.

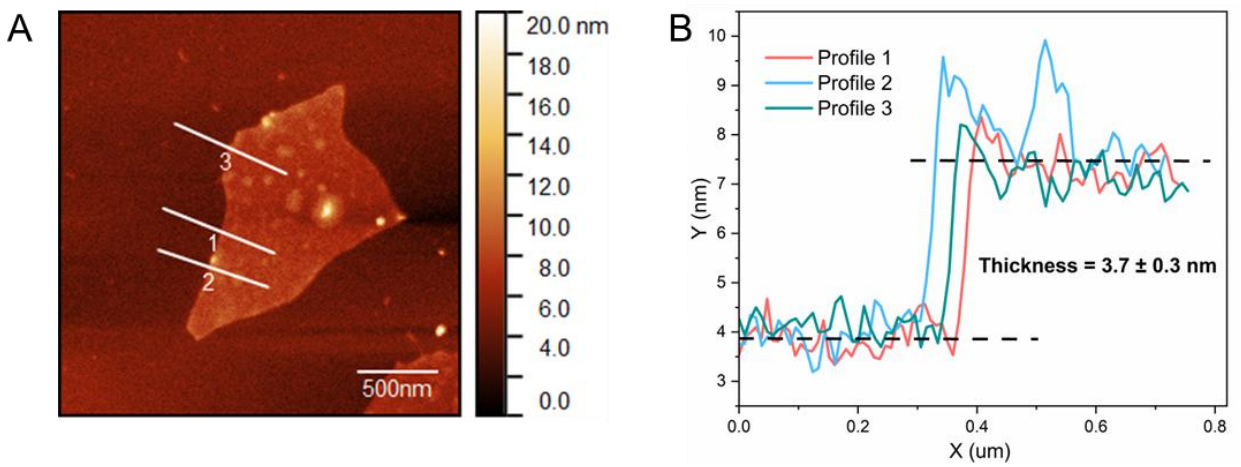

Figure S13. AFM characterization of $Ti_3C_2T_x$ flakes. (a) Representative AFM image of a single $Ti_3C_2T_x$ flake. (b) Height profiles measured along three randomly selected lines across the flake, illustrating its thickness.